Surface plasmon-enhanced x-ray ultraviolet nonlinear interactions

H. Aknin , O. Sefi , D. Borodin , E. Strizhevsky , J.-P. Rueff, 3 J. M. Ablett , and S. Shwartz^{1,*} ¹Physics Department and Institute of Nanotechnology, Bar-Ilan University, Ramat Gan 52900, Israel ²Synchrotron SOLEIL, L'Orme des Merisiers, Départementale 128, 91190 Saint-Aubin, France ³Sorbonne Université, CNRS, Laboratoire de Chimie Physique-Matière et Rayonnement, LCPMR, F-75005 Paris, France

(Received 27 January 2025; accepted 14 October 2025; published 1 December 2025)

We propose and demonstrate a method to manipulate x-ray emission rates and directions by coupling them to surface plasmon polaritons via x-ray-to-ultraviolet down-conversion in a metal. This mechanism generates highly correlated photon pairs, each consisting of one x-ray and one ultraviolet photon, enabling fine control of x-ray angular and spectral characteristics through the ultraviolet photons resonant with the surface plasmons. Our approach bridges a previously insurmountable gap between x-ray and plasmonic energy and momentum, enabling the use of engineered plasmonic structures to control x-ray emission. Furthermore, our work unlocks opportunities to explore plasmonic physics at the microscopic scale with atomic-scale resolution.

DOI: 10.1103/159t-lldy

I. INTRODUCTION

Surface plasmon polaritons (SPPs) are surface waves that propagate along the interface between a metal and a dielectric [1,2]. They have attracted significant attention due to their ability to confine and enhance electromagnetic fields at this boundary [3,4]. Since their discovery, SPPs have been harnessed to control and enhance a wide range of linear and nonlinear optical phenomena [4–6]. Notable examples include the enhancement of spontaneous emission from quantum emitters [7–12] and the amplification of nonlinear optical interactions [12–17]. The spectral and directional properties of SPPs enable strong capability to manipulate light at material interfaces, leading to the development of groundbreaking optical devices [18–25]. Furthermore, the enhanced interactions facilitated by SPPs have enabled the advancement of techniques such as superresolution imaging [26-28] and highly sensitive spectroscopy [26,29–32].

While the field of optics has made remarkable strides in controlling and manipulating light through SPPs and other approaches [1,21,33], translating these capabilities to the xray regime presents significant challenges [34].

Efficient coupling between radiation and plasmons requires matching both energy and momentum. In the optical regime, energy conservation is achieved by matching the surface plasmon resonance frequency with the photon frequency. Momentum conservation demands matching the wave vector of the incident light with that of the SPP, a condition that can be achieved using prisms, gratings, or other optical structures that allow for precise wave vector engineering of

Published by the American Physical Society under the terms of the Creative Commons Attribution 4.0 International license. Further distribution of this work must maintain attribution to the author(s) and the published article's title, journal citation, and DOI.

the incident radiation [1,2,21,35]. However, coupling x-rays to SPPs is particularly challenging due to their extremely high frequency and wave vector, which far exceed the typical plasma frequency and SPP wave vectors. The absence of equivalent optical components to those in the optical range makes the direct matching between the wave vectors of x-rays and SPPs practically impossible. As a result, and despite the immense potential to advance fundamental science and enable applications, such as x-ray microscopy and spectroscopy, experimental demonstrations in this regime remain unrealized.

Here, we propose and demonstrate an approach to control the rate and emission angles of x-ray photons by exploiting the entanglement between x-rays and SPPs in the ultraviolet (UV) range. We leverage spontaneous parametric down-conversion (SPDC) of x-rays into longer-wavelength radiation [36–45] within an aluminum crystal to generate entangled photon pairs. One photon in each pair is an x-ray photon, while the other is a UV photon that can couple to surface plasmons in the crystal, effectively becoming an SPP. While the SPPs are absorbed within the crystal, the entangled x-ray photons emerge and can be detected. As we demonstrate, the rate and emission angle of these x-ray photons are influenced by the properties of the entangled SPPs. This unique relationship enables the imprinting of optical excitations onto the angular and energy spectrum of the x-ray signal, thereby allowing for precise control over their emission rate and direction.

This process occurs in a distinctive regime: Ultraviolet photons in the 50-200 nm range excite polaritons whose effective wavelengths are of similar scale. Importantly, the penetration depth in this regime is extremely shallow, on the order of tens of nanometers, often shorter than the corresponding free-space wavelength. As a result, the interaction is dominated by surface effects, with smaller contribution from the bulk.

However, for x-rays, whose wavelengths are on the order of an angström, the natural physical scale is that of atomic layers. Consequently, even an extremely short penetration depth spans hundreds of atomic planes. As a result, in

^{*}Contact author: shwarts7@biu.ac.il

nonlinear wave mixing processes involving x-rays, as in our case, longitudinal phase matching becomes essential. Yet what may seem like a strict constraint turns into a powerful advantage: The crystal's reciprocal lattice vectors inherently provide the mechanism for satisfying the phase-matching condition, enabling coherent scattering processes that unveil structural information with atomic-scale precision [38,40,41].

II. THEORY OF DOWN CONVERSION OF X-RAY PHOTONS INTO SURFACE PLASMON POLARITONS

In our scheme, an x-ray pump at frequency ω_p generates entangled photon pairs via SPDC, consisting of a signal photon at frequency ω_s and an idler photon at ω_i , satisfying $\omega_p = \omega_s + \omega_i$. We refer to the x-ray photon as the signal and the longer-wavelength photon as the idler. When the idler frequency approaches the surface plasmon resonance and its in-plane momentum matches that of the SPP, strong coupling occurs, and the idler forms an SPP. In our setup, this momentum matching is achieved by adjusting the sample angle relative to the x-ray source.

Because the SPP must satisfy a specific dispersion relation, determined by the dielectric properties of the interface, the allowed momentum and energy of the idler are tightly constrained. Through conservation laws, these constraints are directly transferred to the entangled x-ray photon, effectively imprinting the SPP dispersion onto its emission angle. Thus, the angular distribution of the x-ray photons is not arbitrary, but dictated by the resonance conditions of the SPP. This process can be described using a macroscopic quantum electrodynamics approach, which quantizes the macroscopic Maxwell's equations in a medium [46,47]. We employ this approach to calculate the count rate of the detected x-ray signal photons using

$$\Gamma_s = \langle 0 | \hat{a}_s^{\dagger} \hat{a}_s | 0 \rangle, \tag{1}$$

where \hat{a}_s^{\dagger} and \hat{a}_s are the creation and annihilation operators for the signal mode at the output of the crystal and are related to the corresponding electric field operators \hat{E}_s^{\dagger} and \hat{E}_s via the Poynting theorem. $|0\rangle$ represents a vacuum state for both the signal and idler modes. Note that Eq. (1) here does not vanish since the signal field *annihilation* operator at the output of the nonlinear crystal is proportional to the idler field *creation* operator, integrated over the interaction SPDC length (see the Supplemental Material [48]).

We begin by describing the theoretical model and writing the vectorial wave equation for the electric field operator, $\hat{E}_u(\vec{r}, \omega_u)$, for a lossy, dispersive, and inhomogeneous medium with a current source, \hat{j}_u , oscillating at a frequency ω_u , where u = s, i stands for signal/idler and $\varepsilon(\vec{r}, \omega_u)$ is the position-dependent permittivity:

$$\nabla \times \nabla \times \hat{E}_{u}(\vec{r}, \omega_{u}) - \frac{\omega_{u}^{2}}{c^{2}} \varepsilon(\vec{r}, \omega_{u}) \hat{E}_{u}(\vec{r}, \omega_{u})$$

$$= -i\omega_{u} \mu_{0} \hat{I}_{u}(\vec{r}, \omega_{u}). \tag{2}$$

This equation accounts for linear and nonlinear interactions, as well as loss and quantum noise contributions, and applies to both signal and idler photons/polaritons. However,

for the signal, we can employ the slowly varying envelope approximation, as shown in the Supplemental Material [48].

To model the down-conversion of x-rays into long-wavelength radiation in absorbing media, we adopt a Langevin approach that introduces noise current operators $\hat{j}_{N,u}$ to preserve the commutators [47]. These noise operators are added to the nonlinear current operators $\hat{j}_{NL,u}$, which couple the signal and idler electric field operators through a nonlinear coupling coefficient. The total source current in Eq. (2) is therefore $\hat{j}_u = \hat{j}_{NL,u} + \hat{j}_{N,u}$ (see the Supplemental Material [48]).

The signal and idler electric fields are then found by solving Eq. (2). As the absorption length of the idler's electric field is comparable to or shorter than its wavelength, the contribution of the weak nonlinear interaction to the idler's propagation is negligible compared to that of the Langevin noise. In this case, the vacuum fluctuations of the idler electric field are proportional to the imaginary part of the Green's function, $G(r, r', \omega)$, that solves Eq. (2) (see the Supplemental Material [48]).

In the Supplemental Material [48], we show that the solution of Eq. (2) for the signal electric field relies on the strongly absorbed idler electric field. It then follows that the signal's count rate [Eq. ((1) is related to the abovementioned Green's function via

$$\Gamma_{s} = \int d\omega_{i} \int \frac{d^{2}q_{s}}{(2\pi)^{2}} \frac{\hbar \omega_{i}^{2}}{\pi \epsilon_{0} c^{2}} |C(q_{s}, q_{p}, \omega_{i})|^{2} \frac{q_{i}^{2}}{k_{i}^{2}(\omega_{i})} \times \int_{L}^{0} dz' \int_{L}^{0} dz e^{i\Delta k_{p,s}(z-z')} \text{Im}\{g_{q_{i}}(z, z', \omega_{i})\}, \quad (3)$$

where the integration boundaries for ω_i and q_s are determined by the energy width of the analyzer and the angular acceptance of the detector, respectively. L is the interaction length for coherent SPDC, estimated from the width of the Bragg diffraction curve of the crystal. $k_i(\omega_i)$ is the idler wave vector in the crystal. The transverse wave vectors $q_{j=p,s,i}$ (for pump, signal, and idler) satisfy transverse momentum conservation $\vec{q}_p = \vec{q}_s + \vec{q}_i$. The term $\Delta k_{p,s}$ describes a longitudinal mismatch along the z axis that includes only the pump and signal contributions. It is given by $\Delta k_{p,s} = k_{p,z}(q_p, \omega_{p,0}) +$ $k_{s,z}(q_s, \omega_{p,0} - \omega_i) - G$, where $k_{p,z}$ and $k_{s,z}$ are the longitudinal pump and signal wave vectors, respectively, and G is the reciprocal lattice vector used for phase matching. The contribution of the longitudinal idler wave vector, $e^{ik_{i,z}z}$, is accounted by the Green's function and thus included in the interaction's longitudinal phase matching also (see the Supplemental Material [48]). $C(q_s, q_p, \omega_i)$ is a prefactor, which accounts for the propagation angles of the pump and signal photons and includes the nonlinear coupling coefficient of $\hat{j}_{NL,s}$.

 g_{q_i} is the Fourier transform of the mentioned Green's function $G(r,r',\omega_i)=\int \frac{d^2\vec{q}_i}{(2\pi)^2}e^{i\vec{q}_i\cdot(\vec{\rho}-\vec{\rho}')}g_{q_i}(z,z',\omega_i)$, where $\vec{\rho}$ is the position along the crystal's surface and \vec{q}_i is the idler wave vector parallel to the crystal's surface. The Green's function $g_{q_i}(z,z',\omega_i)$ includes two contributions: one describing the field in an infinite homogeneous medium with the metal's permittivity, $\varepsilon_{\rm m}(\omega_i)$, and the other describing the field reflected from the interface at z=0.

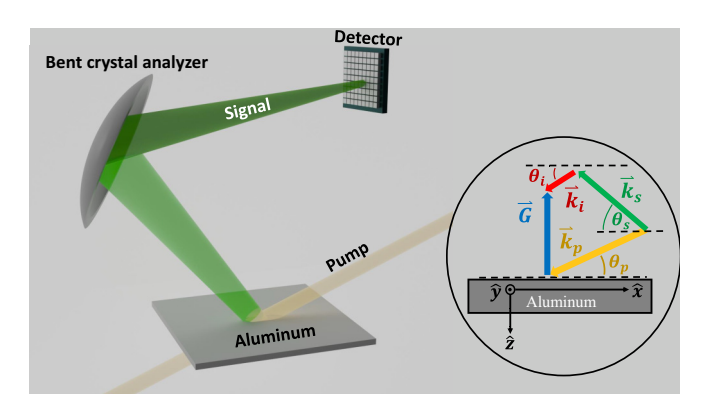


FIG. 1. The experimental setup. A monochromatic x-ray pump beam illuminates the aluminum crystal at an incidence angle θ_p , generating signal photons and either idler photons or polaritons. The angles are measured relative to the atomic planes (dashed lines); the indices p, s, and i stand for the pump, signal, and idler, respectively. A spherically bent crystal analyzer tuned to the signal frequency collects the x-ray signal photons and images them onto the detector. The inset shows a side view of the phase matching diagram with the idler (red) and the reciprocal lattice vector (blue) included.

Since the imaginary part of the Green's function is proportional to the vacuum fluctuations of the idler field, Eq. (3) indicates that the x-ray signal intensity depends directly on the vacuum fluctuations of the long-wavelength idler electric field. According to the fluctuation dissipation theorem, these fluctuations increase with the absorption of the idler field, reaching a maximum when $\hbar\omega_i \approx \hbar\omega_{SPR}$, where SPR stands for surface plasmon resonance. Consequently, from energy conservation, the signal count rate is expected to peak at an energy of $\hbar\omega_s = \hbar\omega_{\text{pump}} - \hbar\omega_{\text{SPR}}$, and the difference in the momentum of the pump and signal x-ray photons, $\vec{q}_p - \vec{q}_s$, follows that of an SPP. Thus, we can alter x-ray pump angle, for example, simply by fixing the detector angle for the x-ray signal photons and tuning the analyzer to pass different signal energies, $\hbar\omega_s$, corresponds to different idler energies ($\hbar\omega_i$ = $\hbar\omega_p - \hbar\omega_s$). The SPP dispersion relation, $q_i(\omega_i)$, will thus be imprinted into the angular profile of the pump x-ray photons.

The boundary conditions of the layered problem are incorporated in the count rate equation [Eq. (3)] via the Green's function solution for the idler electric field, g_{q_i} . This solution for the Maxwell's equations includes the Fresnel reflection coefficient for a p-polarized electric field, which accounts for the boundary condition at the interfaces between the layers (see the layered geometry of Fig. S1 in the Supplemental Material [48]). In Sec. I F of the Supplemental Material [48], we show in detail how the thin oxide layer affects the Fresnel reflection coefficient, and thus the spectrum of the detected x-ray SPDC signal.

III. EXPERIMENTAL SETUP AND PROCEDURE

The experimental setup is depicted in Fig. 1. We used a monochromatic pump beam to illuminate aluminum crystal. The pump photon energy was 9.978 keV for the results shown in Fig. 2 and 10.029 keV for those in Fig. 3. To facilitate the detection of weak SPDC signals emitted over a wide angular range, we employed a spherically bent crystal analyzer and a

2D pixelated x-ray detector. The aluminum crystal, analyzer, and detector were arranged in a Rowland circle geometry in the $\hat{x}-\hat{z}$ plane. This configuration provided both a large collection angle of about 6×10^{-6} sr and a total energy resolution of 1.5 eV FWHM.

We chose high-purity polycrystalline aluminum as our sample, motivated by its relatively high SPR frequency. For metals, the SPR condition is roughly given by $\omega_{\rm SPR} \approx$ $\omega_{\rm plasma}/\sqrt{2}$, which for aluminum yields a resonance near 10 eV [49]. This choice enhances the signal-to-noise ratio in our experiment, as we measure signal photons that are approximately 7–25 eV below the photon energy of the input beam. Given the energy resolution of our experimental setup, we could efficiently filter out noise from Bragg diffraction and Compton-scattered beams, effectively separating the SPRenhanced peak from the elastic peak at energy $\hbar\omega_n$. To detect down-converted x-ray signal photons, we used a near-Bragg geometry, where the signal photons emerge from the same surface of the crystal that the pump photons enter. This is also the surface along which the plasmon polaritons propagate. We denote θ_p and θ_s as the propagation angles of the pump and signal, respectively, with respect to the atomic planes as described in the inset in Fig. 1.

In the experiment, we measured the signal at the detector by varying both the crystal and detector arm angles. The crystal analyzer angle was tuned to select idler photon energies in the range of 6–25 eV for detection. This is achieved by tuning the analyzer to angles corresponding to lower photon energies of the signal, following the energy conservation relation $\hbar\omega_s = \hbar\omega_p - \hbar\omega_i$.

IV. COMPARING THE EXPERIMENTAL RESULTS AGAINST THE THEORY

First, we scanned the sample angle in the vicinity of the Bragg condition and collected the corresponding SPDC signal. Figure 2(a) displays a colormap of the measured signal intensity as a function of idler energy and the pump angle deviation from the Bragg angle, using phase matching with the reciprocal lattice vector normal to the (0, 0, 4) planes. Figure 2(b) shows the corresponding simulation, calculated from Eq. (3).

As observed in Fig. 2(a), the measured pump angle of maximum intensity has a relatively sharp transition around the SPR energy, $\hbar\omega_{\rm SPR}$. Two distinct intensity branches can then be observed below ~ 10 eV and above ~ 15 eV in agreement with our theoretical predictions in Fig. 2(b). The observed angular dependence of the pump beam is a key signature of plasmonic systems and has been observed in other types of measurements [1,17,50]. In our work, this phenomenon arises from phase matching for the SPDC, where, near the SPR resonance, it is governed by the SPP dispersion, while away from resonance, it is determined by normal dispersion.

Next, we plot the signal spectrum by integrating the intensity in Figs. 2(a) and 2(b) over the pump angle for each idler energy. Both theory and experiment indicate that the highest signal intensity occurs at the SPR frequency and gradually decreases for optically radiative modes, i.e., for idler frequencies higher than the bulk plasmon resonance frequency, $\hbar\omega_{BPR} \approx 15.8 \text{ eV}$. The observed angular and energy dependence of the

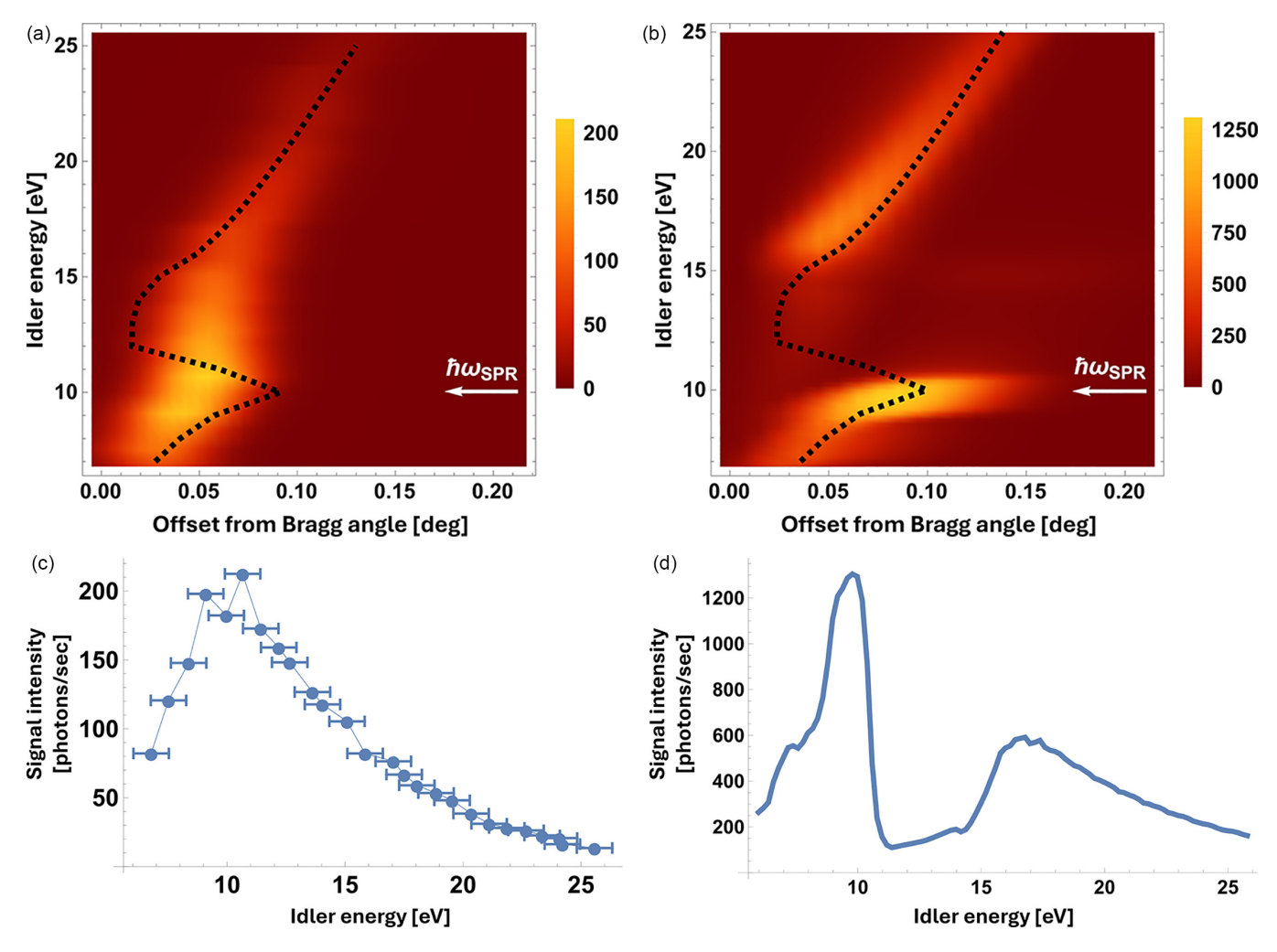


FIG. 2. SPDC of x-rays into UV plasmon polaritons in aluminum, obtained using 9.978 keV pump photons and the reciprocal lattice vector normal to the (0, 0, 4) atomic planes. (a) Experimental results and (b) QED simulation of the signal intensity as a function of the idler photon energy and the deviation of the pump angle from the Bragg angle. The black dots represent the transverse momentum conservation condition, for the pump angle (relative to the Bragg angle), assuming, for simplicity, that the idler follows the SPP dispersion at an aluminum-air interface. It is evident that phase matching is still possible in the energy range between the bound and radiative modes where the intensity of the full QED simulation drops. Panels (c) and (d) show the signal intensity as a function of the idler photon energy. (c) Dots represent experimental results and (d) line represents simulation. (c) The horizontal error bars represent the experimental energy uncertainty, which corresponds to the total energy resolution. The vertical error is smaller than the point size.

x-ray photons provides clear experimental evidence for the existence of SPPs and their coupling to the x-ray photons.

We note that in the simulations we observed a second peak, which is located near the bulk plasma resonance energy. This feature arises from a completely different mechanism. At the bulk plasma resonance, the real part of the metal's permittivity approaches zero, causing the SPDC count rate to diverge, as predicted by Eq. (3). However, this divergence is suppressed by the short coherence length of the SPDC interaction, which, as discussed in the discussion below, is no larger than 60 nm.

Following the observation of SPDC of x-ray photons into SPPs from the (0, 0, 4) atomic planes, we sought to verify that this enhancement near the SPR was not a coincidental feature of a particular reflection or pump energy. To that end, we performed measurements for the Al(1, 1, 1) and Al(0, 0, 2) reflections at a pump photon energy of 10.029 keV. As shown in Fig. 3, similar SPDC behavior was observed, confirming

the robustness of the effect across multiple crystallographic orientations.

To further confirm that the enhancement is independent of detector alignment, we conducted measurements at different detector angles. Here, we fixed the pump angle at a detuning of 0.19° from the Bragg condition and performed a scan over the detector arm's angle to collect the SPDC signal. The experimental spectra for Al(1, 1, 1) and Al(0, 0, 2) are shown in Figs. 3(a) and 3(b), respectively, while the corresponding simulations based on Eq. (3) are presented in Figs. 3(c) and 3(d), respectively.

As shown in the experimental spectra in Figs. 3(a) and 3(b), an enhancement appears at a signal energy $\hbar\omega_{SPR}=10.6$ eV below the pump energy of 10.029 keV. This observation is consistent with the observation for the Al(0, 0, 4) atomic planes using a pump energy of 9.978 keV, as demonstrated in Fig. 2.

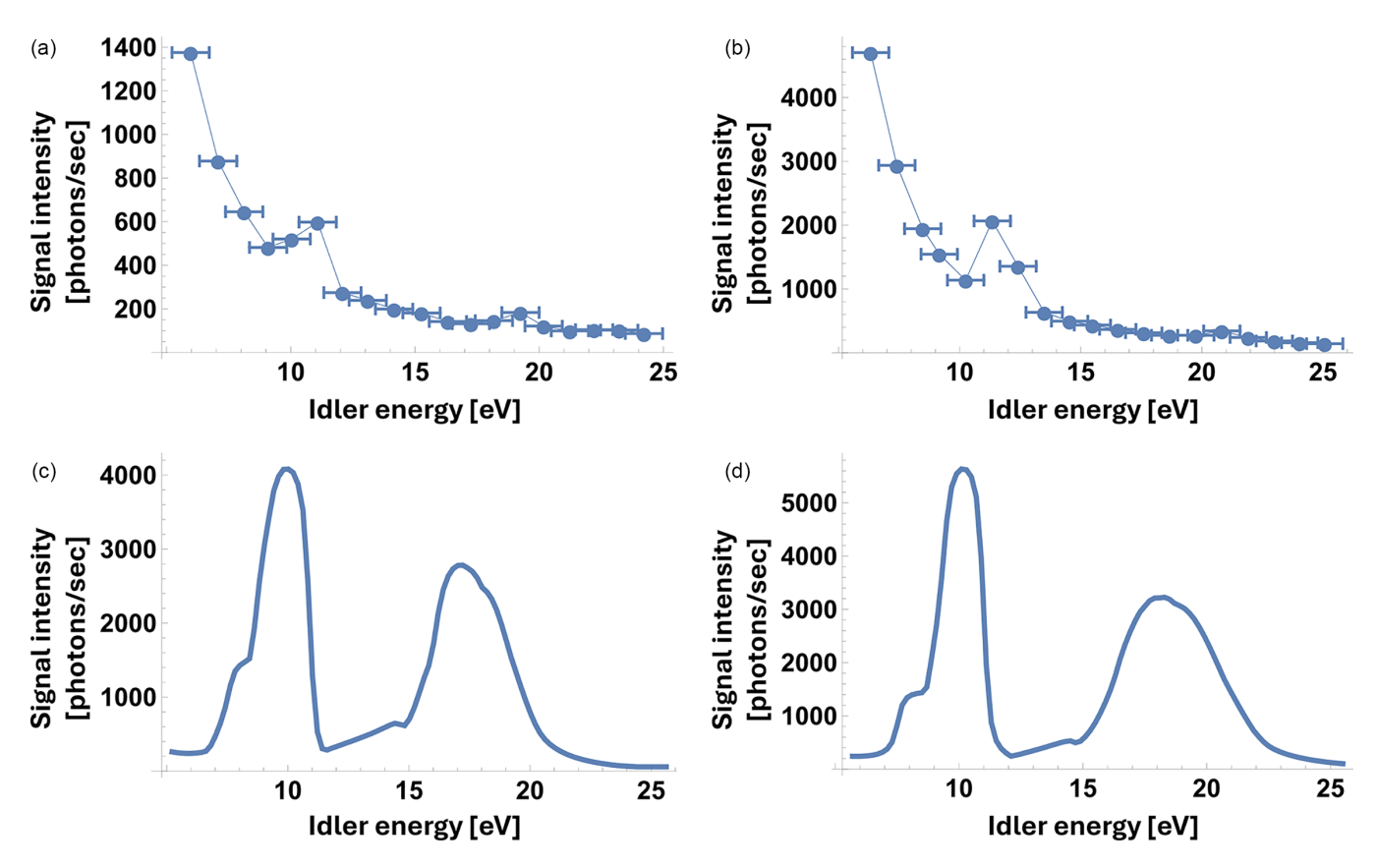


FIG. 3. Experimental [panels (a) and (b)] and simulated [panels (c) and (d)] signal spectra for the Al(1, 1, 1) and Al(0, 0, 2) atomic planes, obtained using 10.029 keV pump photons. The horizontal error bars in panels (a) and (b) represent the experimental energy uncertainty, which corresponds to the total energy resolution. The vertical error is smaller than the point size. See the text for additional details.

The similarity between the experimental spectra of the Al(1, 1, 1) and Al(0, 0, 2) reflections [Figs. 3(a) and 3(b)] arises due to the common pump angle deviation and the similarity of the reciprocal lattice vector used for those measurements This similarity is well captured in the corresponding QED simulations [Figs. 3(c) and 3(d)], which also reveal a second, weaker feature near the bulk plasma energy, a signature that is faint but discernible in the experimental data as well.

Taken together, Figs. 2 and 3 exhibit good qualitative agreement between experiment and theory near the surface plasmon resonance. Both clearly demonstrate that SPDC is enhanced when the signal photon energy falls below the pump energy by an amount corresponding to SPR energy, in accordance with the theoretical predictions.

In the experimental spectra presented in Figs. 3(a) and 3(b), the SPR-related peaks appear on top of a slowly decreasing background, originating from the residual tail of the Bragg-diffracted signal that was not fully suppressed by our setup and analysis. Nevertheless, the SPR-induced enhancement remains unambiguous.

The measured peak widths are slightly broader than predicted, primarily due to uncertainties in beam bandwidth, analyzer resolution, and beam divergence. In addition, crystal mosaicity plays a key role. Although not precisely measured, the observed Bragg curve widths of $0.17^{\circ}-0.21^{\circ}$ suggest low crystalline quality and a coherence length no greater than $\sim\!60$ nm. This short coherence length reduces

the efficiency of bulk SPDC, which is more sensitive to interaction length than surface generation [17] and explains the relatively weak enhancement near the bulk plasma frequency.

Further deviations between experiment and theory stem from uncertainties in the optical parameters used. While the thickness of the oxide layer varies across studies, it typically ranges from 1.2 to 5 nm [51–53], and its properties deviate from those of bulk alumina due to its amorphous and inhomogeneous nature. The dielectric constants of ultrathin aluminum oxide films remain poorly characterized in the literature. A detailed discussion of their influence on the SPR and SPDC enhancement is provided in Sec. IE of the Supplemental Material [48]. Importantly, these uncertainties affect only secondary features and do not alter the primary prediction: The surface plasmonmediated enhancement of the x-ray SPDC signal is robust and clearly observed.

V. CONCLUSIONS

In conclusion, we have presented a method for controlling x-ray flux and emission angles through entanglement with longer-wavelength photons, which efficiently interact with surface plasmons. Although the entanglement cannot be directly measured, since the SPP cannot emerge from the crystal, the strong correlation between the SPP and the entangled x-ray photon persists. As a result, the rate and emission angle of the x-rays are controlled by the properties of the SPP

Enhanced surface control would allow greater precision in regulating the emitted signal count rate and emission angles. This can be achieved through nanofabrication techniques commonly used in metamaterials and nano-optics [16,50]. Furthermore, as x-rays are highly sensitive to local fields with atomic-scale resolution, our method opens frontiers for studying the effects of nanofabrication on local fields in a noninvasive manner. This information, currently inaccessible, could significantly enhance the understanding of nanostructure functionality and offers valuable insights into their optimization.

- [1] S. A. Maier, *Plasmonics: Fundamentals and Applications*, 1st ed. (Springer, New York, 2007).
- [2] H. Raether, G. Hohler, and E. A. Niekisch, Surface Plasmons on Smooth and Rough Surfaces and on Gratings, Springer Tracts in Modern Physics Vol. 111 (Springer-Verlag, Berlin, Heidelberg, 1988).
- [3] R. H. Ritchie, Plasma losses by fast electrons in thin films, Phys. Rev. 106, 874 (1957).
- [4] F. J. Garcia-Vidal, A. I. Fernández-Domínguez, L. Martin-Moreno, H. C. Zhang, W. Tang, R. Peng, and T. J. Cui, Spoof surface plasmon photonics, Rev. Mod. Phys. 94, 025004 (2022).
- [5] H. Yu, Y. Peng, Y. Yang, and Z. Y. Li, Plasmon-enhanced lightmatter interactions and applications, npj Comput. Mater. 5, 45 (2019).
- [6] M. I. Stockman *et al.*, Roadmap on plasmonics, J. Opt. 20, 043001 (2018).
- [7] J. Moreland, A. Adams, and P. K. Hansma, Efficiency of light emission from surface plasmons, Phys. Rev. B 25, 2297 (1982).
- [8] K. Kneipp, Y. Wang, H. Kneipp, L. T. Perelman, I. Itzkan, R. R. Dasari, and M. S. Feld, Single molecule detection using surface-enhanced Raman scattering (SERS), Phys. Rev. Lett. 78, 1667 (1997).
- [9] K. Okamoto, I. Niki, A. Shvartser, Y. Narukawa, T. Mukai, and A. Scherer, Surface-plasmon-enhanced light emitters based on InGaN quantum wells, Nat. Mater. 3, 601 (2004).
- [10] G. Sun, J. B. Khurgin, and R. A. Soref, Practicable enhancement of spontaneous emission using surface plasmons, Appl. Phys. Lett. **90**, 111107 (2007).
- [11] E. Fort and S. Grésillon, Surface enhanced fluorescence, J. Phys. D: Appl. Phys. 41, 013001 (2007).
- [12] K. A. Ivanov, K. M. Morozov, G. Pozina, A. R. Gubaydullin, E. I. Girshova, and M. A. Kaliteevski, Control of the surface plasmon dispersion and Purcell effect at the metamaterialdielectric interface, Sci. Rep. 10, 20828 (2020).
- [13] R. Reinisch and M. Nevière, Electromagnetic theory of diffraction in nonlinear optics and surface-enhanced nonlinear optical effects, Phys. Rev. B **28**, 1870 (1983).
- [14] C. K. Chen, A. R. B. De Castro, and Y. R. Shen, Surface-enhanced second-harmonic generation, Phys. Rev. Lett. 46, 145 (1981).
- [15] J. C. Quail, J. G. Rako, H. J. Simon, and R. T. Deck, Optical second-harmonic generation with long-range surface plasmons, Phys. Rev. Lett. **50**, 1987 (1983).

ACKNOWLEDGMENT

This work was supported by the Israel Science Foundation (ISF) (IL), Grant No. 2208/24.

DATA AVAILABILITY

The data that support the findings of this article are not publicly available upon publication because it is not technically feasible and/or the cost of preparing, depositing, and hosting the data would be prohibitive within the terms of this research project. The data are available from the authors upon reasonable request.

- [16] M. Kauranen and A. V. Zayats, Nonlinear plasmonics, Nat. Photon. 6, 737 (2012).
- [17] Y. R. Shen, *Principles of Nonlinear Optics* (John Wiley & Sons, New York, 1873), Vol. 1.
- [18] X. Ni, N. K. Emani, A. V. Kildishev, A. Boltasseva, and V. M. Shalaev, Broadband light bending with plasmonic nanoantennas, Science **335**, 427 (2012).
- [19] M. Hong, R. B. Dawkins, B. Bertoni, C. You, and O. S. Magaña-Loaiza, Nonclassical near-field dynamics of surface plasmons, Nat. Phys. 20, 830 (2024).
- [20] I. Dolev, I. Epstein, and A. Arie, Surface-plasmon holographic beam shaping, Phys. Rev. Lett. 109, 203903 (2012).
- [21] W. L. Barnes, A. Dereux, and T. W. Ebbesen, Surface plasmon subwavelength optics, Nature (London) 424, 824 (2003).
- [22] J. B. Pendry, L. Martín-Moreno, and F. J. Garcia-Vidal, Mimicking surface plasmons with structured surfaces, Science 305, 847 (2004).
- [23] A. V. Kildishev, T. A. Klar, V. P. Drachev, and V. M. Shalaev, Thin metal-dielectric nanocomposites with a negative index of refraction, in *Nanophotonics with Surface Plasmons*, edited by V. M. Shalaev and S. G. Moiseev (Elsevier, Amsterdam, 2007), p. 271.
- [24] G. Kumar and P. K. Sarswat, *Interaction of Surface Plasmon Polaritons with Nanomaterials*, edited by C. D. Geddes (Springer, Cham, Switzerland, 2016), pp. 103–129.
- [25] J. A. Schuller, E. S. Barnard, W. Cai, Y. C. Jun, J. S. White, and M. L. Brongersma, Plasmonics for extreme light concentration and manipulation, Nat. Mater. 9, 193 (2010).
- [26] P. K. Jain, X. Huang, I. H. El-Sayed, and M. A. El-Sayed, Noble metals on the nanoscale: Optical and photothermal properties and some applications in imaging, sensing, biology, and medicine, Acc. Chem. Res. 41, 1578 (2008).
- [27] J. Homola, S. S. Yee, and G. Gauglitz, Surface plasmon resonance sensors: Review, Sens. Actuat. B 54, 3 (1999).
- [28] A. V. Zayats and I. I. Smolyaninov, Near-field photonics: Surface plasmon polaritons and localized surfaceplasmons, J. Opt. A: Pure Appl. Opt. 5, S16 (2003).
- [29] C. K. Chen, A. R. B. De Castro, Y. R. Shen, and F. DeMartini, Surface coherent anti-Stokes Raman spectroscopy, Phys. Rev. Lett. 43, 946 (1979).
- [30] S. Nie and S. R. Emory, Probing single molecules and single nanoparticles by surface-enhanced Raman scattering, Science 275, 1102 (1997).

- [31] K. A. Willets and R. P. Van Duyne, Localized surface plasmon resonance spectroscopy and sensing, Annu. Rev. Phys. Chem. **58**, 267 (2007).
- [32] X. Wang, S. C. Huang, S. Hu, S. Yan, and B. Ren, Fundamental understanding and applications of plasmon-enhanced Raman spectroscopy, Nat. Rev. Phys. 2, 253 (2020).
- [33] D. K. Gramotnev and S. I. Bozhevolnyi, Plasmonics beyond the diffraction limit, Nat. Photon. 4, 83 (2010).
- [34] R. Röhlsberger, J. Evers, and S. Shwartz, Quantum and nonlinear optics with hard x-rays, in *Synchrotron Light Sources* and Free-Electron Lasers: Accelerator Physics, Instrumentation and Science Applications, edited by E. Jaeschke, S. Khan, J. R. Schneider, and J. B. Hastings (Springer, Cham, Switzerland, 2020), p. 1399.
- [35] E. Kretschmann and H. Raether, Radiative decay of non radiative surface plasmons excited by light, Z. Naturforsch. A 23, 2135 (1968).
- [36] H. Danino and I. Freund, Parametric down conversion of x rays into the extreme ultraviolet, Phys. Rev. Lett. **46**, 1127 (1981).
- [37] K. Tamasaku, K. Sawada, E. Nishibori, and T. Ishikawa, Visualizing the local optical response to extreme-ultraviolet radiation with a resolution of $\lambda/380$, Nat. Phys. 7, 705 (2011).
- [38] D. Borodin, S. Levy, and S. Shwartz, High energy-resolution measurements of x-ray into ultraviolet parametric down-conversion with an x-ray tube source, Appl. Phys. Lett. **110**, 131101 (2017).
- [39] S. Sofer, O. Sefi, E. Strizhevsky, H. Aknin, S. P. Collins, G. Nisbet, B. Detlefs, C. J. Sahle, and S. Shwartz, Observation of strong nonlinear interactions in parametric down-conversion of X-rays into ultraviolet radiation, Nat. Commun. 10, 5673 (2019).
- [40] A. Schori, C. Bömer, D. Borodin, S. P. Collins, B. Detlefs, M. Moretti Sala, S. Yudovich, and S. Shwartz, Parametric down-conversion of x rays into the optical regime, Phys. Rev. Lett. 119, 253902 (2017).
- [41] D. Borodin, A. Schori, J. P. Rueff, J. M. Ablett, and S. Shwartz, Evidence for collective nonlinear interactions in x ray into

- ultraviolet parametric down-conversion, Phys. Rev. Lett. **122**, 023902 (2019).
- [42] R. Cohen and S. Shwartz, Theory of nonlinear interactions between x rays and optical radiation in crystals, Phys. Rev. Res. 1, 033133 (2019).
- [43] K. Tamasaku and T. Ishikawa, Interference between compton scattering and X-ray parametric down-conversion, Phys. Rev. Lett. 98, 244801 (2007).
- [44] K. Tamasaku, K. Sawada, and T. Ishikawa, Determining X-ray nonlinear susceptibility of diamond by the optical Fano effect, Phys. Rev. Lett. **103**, 254801 (2009).
- [45] B. Barbiellini, Y. Joly, and K. Tamasaku, Explaining the x-ray nonlinear susceptibility of diamond and silicon near absorption edges, Phys. Rev. B 92, 155119 (2015).
- [46] N. Rivera and I. Kaminer, Light-matter interactions with photonic quasiparticles, Nat. Rev. Phys. 2, 538 (2020).
- [47] S. Scheel and S. Y. Buhmann, Macroscopic quantum electrodynamics—Concepts and applications, Acta Phys. Slov. **58**, 675 (2008).
- [48] See Supplemental Material at http://link.aps.org/supplemental/ 10.1103/l59t-lldy for experimental and theoretical supplemental information.
- [49] F. Pellerin, C. Le Gressus, and D. Massignon, A secondary electron spectroscopy and electron energy loss spectroscopy study of the interaction of oxygen with a polycrystalline aluminum surface, Surf. Sci. 103, 510 (1981).
- [50] L. Novotny and B. Hecht, *Principles of Nano-Optics* (Cambridge University Press, Cambridge, 2012).
- [51] P. Dumas, J. P. Dubarry-Barbe, D. Riviere, Y. Levy, and J. Corset, Growth of thin alumina film on aluminium at room temperature: A kinetic and spectroscopic study by surface plasmon excitation, J Phys. Colloq. 44, C10 (1983).
- [52] J. D. Baran, H. Grönbeck, and A. Hellman, Mechanism for limiting thickness of thin oxide films on aluminum, Phys. Rev. Lett. 112, 146103 (2014).
- [53] J. J. Cowan and E. T. Arakawa, Dispersion of surface plasmons in dielectric-metal coatings on concave diffraction gratings, Z. Phys. 235, 97 (1970).